Premature bearing failure in lightly built rotating machinery induced by housing compliance: Experimental evidence and contact-mechanics analysis from a ceiling fan system

Neha Pandey [a] and Deepak K. Pandey [b*]
[a] Department of Applied Mechanics, Indian Institute of Technology Delhi, New Delhi-110016, India
[b] Designing Alley, New Delhi-110016, India
*Email: pdk201994@gmail.com

Abstract

Premature bearing failures are frequently reported in lightly built rotating machinery such as ceiling fans, despite the use of high-quality rolling element bearings and the absence of classical rolling-contact fatigue damage. Field inspections typically reveal fretting marks on bearing outer races, lubricant discoloration, elevated vibration levels, and localized heating near bearing housings, yet conventional vibration-based diagnostics fail to identify discrete fault signatures. This study investigates the hidden structural cause of such failures through combined experimental measurements and numerical contact-mechanics analysis using a commercially representative ceiling fan system. Bearing housing support rigidity was systematically varied by modifying housing thickness, spot-weld density, and rib reinforcement. Experimental results show that compliant housing configurations exhibit 40–60% higher RMS vibration levels and bearing housing temperature rises of 8–12°C compared with reinforced configurations under identical operating conditions. Finite element analysis reveals that reduced housing stiffness produces non-axisymmetric bearing seat ovalisation, resulting in highly non-uniform contact pressure distributions and peak contact stress increases of approximately 30%. These pressure gradients promote micro-slip and fretting-type behaviour at the bearing–housing interface, generating frictional heat and broadband vibration amplification rather than classical defect frequencies. The combined evidence establishes housing compliance as a primary root cause of premature bearing degradation in lightly supported rotating systems. The findings explain why such failures are often misattributed to bearing quality and why traditional fault-frequency diagnostics are ineffective. Structural reinforcement of bearing housings is shown to be a more effective reliability measure than modification of bearing clearance or replacement of bearings.

Keywords: Bearing failure analysis; Housing compliance; Fretting; Contact instability; Thermo-mechanical degradation; Ceiling fan

1. Introduction

Premature bearing failures are frequently reported in lightly built rotating machinery used in domestic and commercial applications, including ceiling fans [1,2], exhaust fans [3], and small electric motors. These failures often occur well before the predicted rolling-contact fatigue life [4] of the bearings is reached, even when high-quality bearings from reputable manufacturers are used. Field inspections of failed units commonly reveal fretting marks on the bearing outer race, lubricant discoloration, abnormal vibration, and localized heating near the bearing housings. However, classical fatigue indicators such as spalling, pitting, or raceway cracking are often absent. This discrepancy indicates that the degradation mechanism in such systems differs fundamentally from conventional rolling-contact fatigue described in bearing literature [5–8].

In industrial practice, these failures are typically diagnosed using vibration-based fault detection methods developed for rolling element bearings. Such methods rely on the presence of characteristic defect frequencies associated with localized damage on races or rolling elements [3,4,6,7,9,10]. In many lightly supported rotating systems, however, vibration spectra instead exhibit broadband energy amplification without distinct fault signatures [4]. As a result, premature failures are frequently misattributed to bearing quality, lubrication issues, or manufacturing variability. Replacing the bearing often fails to resolve the problem, indicating that the root cause lies in the supporting structure rather than in the bearing itself.

One structural feature common to such machinery is the use of thin sheet-metal bearing housings assembled using spot welding or minimal reinforcement. Bearings are mounted using interference fits intended to prevent slip and ensure proper seating. While economically attractive, this construction introduces the possibility that the bearing housing is sufficiently compliant to deform elastically under assembly preload and operational loads. From a mechanics perspective, such deformation can distort the bearing seat, produce non-uniform contact pressure at the bearing–housing interface, and restrict thermal expansion of the bearing outer race. These effects are not considered in conventional bearing life calculations, which assume rigid and axisymmetric support conditions [7,11].

Contact-mechanics studies show that non-uniform support and high local contact pressures can promote micro-slip and fretting behaviour at interfaces subjected to cyclic loading. Fretting is known to generate frictional heat, surface damage, and debris that accelerate lubricant degradation and alter contact conditions over time [12–14]. In the context of rolling element bearings, such behaviour can occur at the bearing–housing interface when circumferential support is non-uniform. Under sustained operation, this may produce elevated temperatures, increasing effective preload within the bearing and shifting lubrication from full-film to mixed or boundary regimes. These coupled thermo-mechanical effects are capable of degrading bearing performance without producing classical fatigue damage [15].

Despite its practical importance, the influence of bearing housing structural compliance on bearing degradation has received very limited attention in the literature. Research on ceiling fans and similar devices has predominantly focused on airflow characteristics, thermal comfort, aerodynamic optimisation, motor efficiency, and noise reduction [16–19]. Very little work has examined how housing stiffness, bearing seating conditions, and assembly practices influence vibration response and thermal behaviour of the bearing system. Consequently, premature bearing failures in such equipment are rarely analysed from a structural standpoint.

The present study investigates this overlooked failure mechanism using a commercially representative ceiling fan as a test platform. Ceiling fans provide an ideal system for such investigation because they represent lightly damped rotating machinery with thin sheet-metal bearing supports, long operating durations, and frequent reports of bearing-related vibration and heating issues in service. Housing stiffness is systematically varied by modifying sheet thickness, spot-weld density, and rib reinforcement. Experimental measurements of vibration response and bearing housing temperature rise are conducted under steady operating conditions. Finite element contact analysis is employed to quantify housing deformation, bearing seat ovalisation, and resulting contact pressure non-uniformity under realistic assembly and operational loads.

The objective of this work is not to optimise vibration performance, but to identify the structural root cause of premature bearing degradation in lightly built rotating systems. By integrating experimental evidence with contact-mechanics analysis, this study demonstrates why conventional fault-frequency diagnostics fail in such systems and shows that structural reinforcement of bearing housings is a more effective reliability measure than modification of bearing clearance or repeated bearing replacement. The remainder of this paper is organised as follows. Section 2 describes the experimental and numerical methodology adopted for investigating housing compliance effects. Section 3 presents the combined numerical and experimental results and establishes the failure mechanism linking housing deformation to vibration and thermal behaviour. Section 4 discusses the coupled thermo-mechanical degradation process and its implications for bearing diagnostics and design. Section 5 summarises the principal conclusions and practical recommendations for preventing premature bearing failures in lightly built rotating machinery.

2. Methodology

This section describes the experimental and numerical methodology adopted to reproduce and investigate the premature bearing degradation observed in lightly built ceiling fan assemblies. The methodology was designed to replicate realistic assembly practices and operating conditions encountered in consumer applications, while systematically isolating the effects of housing stiffness, interference fit, and structural reinforcement on stress distribution, elastic deformation, vibration

magnitude, and bearing–housing temperature rise. The overall workflow integrates geometric characterisation, controlled experimental measurements, and finite element contact analysis, enabling direct correlation between housing deformation mechanisms and the failure symptoms observed in service.

2.1. Ceiling fan assembly and bearing housing configuration

The investigated ceiling fan corresponds to a commercially representative, low-cost design widely used in residential applications. The assembly comprises a single-phase induction motor, a vertical steel shaft, an upper and a lower deep-groove ball bearing, upper and lower bearing housings integrated into the fan covers, and a blade hub, as shown schematically in Figure 1. The bearings support the rotor shaft and transmit dynamic loads to the surrounding sheet-metal housings, which serve as the primary structural interfaces between the rotating and stationary components.

The lower bearing housing is manufactured from thin steel sheet and is attached to the lower cover using resistance spot welding. To vary housing stiffness in a controlled manner, two spot-weld configurations were investigated: three and six welds, uniformly distributed along the housing circumference. These configurations represent commonly used manufacturing practices in low-cost fan assemblies and provide distinct levels of structural rigidity while maintaining identical geometry and material properties. The reduced weld configuration is expected to permit increased elastic deformation of the housing under bearing loads, while the higher weld density provides enhanced constraint and stiffness. The upper bearing housing is integrated into the upper cover and, depending on configuration, incorporates circumferential and radial stiffening ribs designed to increase structural rigidity. Both rib-reinforced and non-reinforced upper-cover configurations were examined. Figure 2 presents detailed views of the upper and lower bearing housing geometries, spot-weld locations, and rib layouts. Together, the lower housing weld density and upper cover rib reinforcement define the effective stiffness of the bearing support system and govern load transmission from the rotating shaft–bearing assembly to the stationary structure.

By systematically varying spot-weld density in the lower housing and rib reinforcement in the upper cover, a set of housing configurations spanning a wide range of structural compliance was established. These configurations form the basis for both experimental testing and numerical analysis, enabling isolation of housing stiffness effects on vibration magnitude, thermal response, and bearing support behaviour under otherwise identical operating conditions.

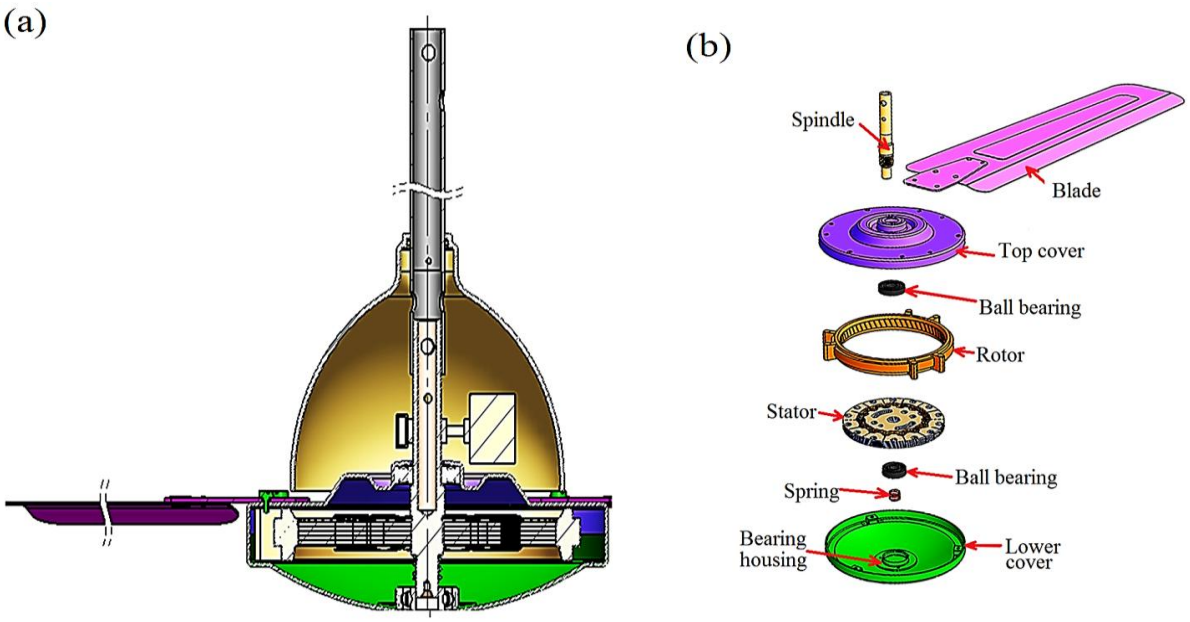

Figure 1: (a) Sectional view of the ceiling fan assembly showing bearing locations; (b) exploded view of the ceiling fan components.

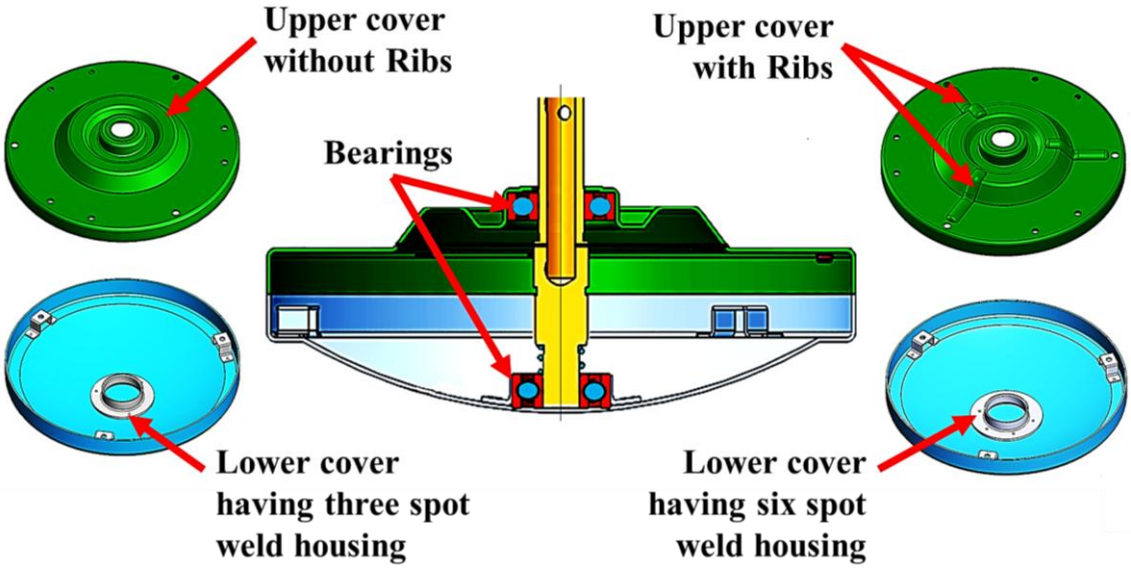

Figure 2: Upper and lower bearing housing configurations showing spot-weld locations and rib reinforcement used to vary structural stiffness.

2.2. Experimental investigation

2.2.1. Vibration and temperature measurements

The experimental programme was designed to quantify the vibration response and bearing-housing temperature rise under steady-state operating conditions. Vibration measurements were performed using piezoelectric accelerometers mounted directly on the upper and lower bearing housings along mutually orthogonal directions to capture vibration associated with bearing–housing interaction and structural compliance effects. Accelerometer mounting locations were selected to ensure good mechanical coupling while avoiding interference with housing deformation.

Vibration response was quantified using the root-mean-square (RMS) acceleration, a_{rms}, calculated over fixed time windows once steady-state operation was achieved. RMS acceleration was selected as a robust broadband metric capable of capturing changes in vibration magnitude arising from stiffness modulation and housing compliance effects, rather than relying on discrete spectral features alone. Bearing-housing temperature was measured using Type-K thermocouples attached directly to the external surfaces of the upper and lower bearing housings using thermally conductive adhesive. Temperature rise was defined as the difference between the measured housing temperature and the ambient temperature recorded at the start of each test. This approach allows direct comparison of thermal behaviour across different housing configurations and bearing clearance classes.

All experiments were conducted at the rated operating speed of the fan under no-load conditions to isolate the influence of housing compliance and bearing characteristics from aerodynamic loading effects. Data acquisition commenced only after vibration and temperature signals reached steady values, thereby minimizing transient effects and ensuring repeatability. Table 1 summarises the instrumentation used, measured parameters, and associated measurement accuracy.

Table 1: Combination of ceiling fan's cover with different ball bearing clearances

Instrument	Parameter measured	Measurement range	Accuracy
Laser tachometer	Rotational speed		± 0.02%
Vibration meter	RMS velocity	0.1 – 400 mm/s	± (5% + 2 digits)
K-type thermocouple	Temperature	-50 to 400 °C	± (0.75% + 2.5 °C)
Energy meter	Power consumption	0 – 3680 W	±2%

2.2.2. Test matrix and operating protocol

Table 2 summarises the experimental test matrix, which includes combinations of bearing housing thickness, spot-weld configuration, upper-cover rib reinforcement, and bearing internal clearance class (CN and C3). SKF 6201 and SKF 6202 deep-groove ball bearings were used for the lower and upper bearing locations, respectively, reflecting common industrial practice in ceiling fan assemblies.

Each experimental configuration was operated continuously for 60 minutes to ensure attainment of steady-state thermal conditions. Ambient temperature was recorded prior to each test. Vibration and temperature data were acquired at 20-minute intervals to capture the time evolution of the response during sustained operation. To ensure repeatability, each configuration was tested three times under identical conditions. The reported results represent averaged values across repeated tests, with observed variability remaining within ±5% for vibration measurements and ±2 °C for temperature measurements.

Table 2: Experimental test matrix for bearing housing configurations and bearing clearances

S. No.	Ball Bearing	Clearances	Lower bearing housing	Upper bearing housing
1.	SKF 6201 / SKF 6202	CN	3 spot welds	No rib
2.	SKF 6201 / SKF 6202	C3		
3.	SKF 6201 / SKF 6202	CN	3 spot welds	3 Ribs
4.	SKF 6201 / SKF 6202	C3		
5.	SKF 6201 / SKF 6202	CN	6 spot welds	No rib
6.	SKF 6201 / SKF 6202	C3		
7.	SKF 6201 / SKF 6202	CN	6 spot welds	3 Ribs
8.	SKF 6201 / SKF 6202	C3		

2.3. Geometric characterization and interference fit evaluation

Geometric dimensions of the upper and lower bearing housings are summarised in Table 3, including housing inner diameter, wall thickness, and outer diameter. Nominal bearing dimensions and tolerances provided by the manufacturer are listed in Tables 4 and 5 for SKF 6201 and SKF 6202 bearings, respectively. These dimensional measurements were obtained using calibrated precision instruments and reflect the as-assembled condition of the components.

The measured housing and bearing dimensions were used to calculate the interference fit between the bearing outer race and the housing bore for each configuration. These interference values govern contact pressure distribution, thermal expansion behaviour, and load transfer at the bearing–housing interface. The calculated interference fits were subsequently used as direct inputs to the numerical contact analysis and to support interpretation of experimentally observed vibration and temperature trends. This procedure ensures consistency and traceability between experimental measurements and numerical simulations.

Table 3: Lower and upper cover bearing houses dimensions

S. No.	Component	Inner Diameter of Bearing Housing (mm)	Thickness of Housing (mm)	Outer Diameter of Bearing Housing (mm)
1.	Lower housing with 3 spot welds	31.835	1.295	33.130
2.	Upper housing without rib	34.817	1.300	36.117
3.	Lower housing with 6 spot welds	31.727	1.635	33.362
4.	Upper housing with rib	34.762	1.300	36.062

Table 4. Diameter dimensions of SKF 6201 ball bearings

S. No.	Condition	Clearance	Inner Diameter (mm)	Outer Diameter (mm)
1.	3 spot welds in the lower bearing housing and no rib on the upper cover	CN	11.93	31.96
2.		C3	11.94	31.94
3.	3 spot welds in the lower bearing housing and rib on upper cover	CN	11.92	31.96
4.		C3	11.95	31.95
5.	6 spot welds in the lower bearing housing and no rib on the upper cover	CN	11.94	32.00
6.		C3	11.93	31.96
7.	6 spot welds in the lower bearing housing and rib on upper cover	CN	11.98	32.01
8.		C3	11.96	31.91

Table 5. Diameter dimensions of SKF 6202 ball bearings

S. No.	Condition	Clearance	Inner Diameter (mm)	Outer Diameter (mm)
1.	3 spot welds in the lower bearing housing and no rib on the upper cover	CN	14.94	34.99
2.		C3	15.00	35.00
3.	3 spot welds in the lower bearing housing and rib on upper cover	CN	14.95	34.95
4.		C3	14.96	34.95
5.	6 spot welds in the lower bearing housing and no rib on the upper cover	CN	14.94	35.02
6.		C3	14.97	34.96
7.	6 spot welds in the lower bearing housing and rib on the upper cover	CN	14.95	35.06
8.		C3	14.95	35.06

2.4. Numerical simulation approach

2.4.1. Finite element model description

Finite element models corresponding to the experimentally investigated configurations were developed to quantify housing stress distribution, elastic deformation, and bearing seat distortion under combined assembly and operational loading. Three-dimensional models of the upper and lower bearing housings were constructed using the ANSYS Structural module. Housing geometries were reconstructed directly from experimentally measured dimensions (Table 3), ensuring geometric fidelity to the manufactured components and direct comparability with experimental observations.

Both bearing housings were modelled using cold-rolled close-annealed (CRCA) steel, assumed to be homogeneous, isotropic, and linearly elastic. This assumption is justified by the absence of observable plastic deformation under normal assembly and operating conditions. Bearing outer races were modelled as rigid bodies, while the housings were treated as deformable solids. This modelling approach is appropriate when housing compliance dominates the deformation response and enables efficient yet accurate prediction of housing behaviour [7]. Surface-to-surface frictional contact was defined between the bearing outer race and the housing bore to capture non-uniform contact pressure distributions, local stress concentrations, and elastic seat ovalisation. These effects are critical for understanding stiffness modulation and vibration amplification mechanisms observed experimentally.

2.4.2. Loading and boundary conditions

The finite element models were subjected to loading and boundary conditions representative of bearing assembly and steady-state operation. Radial interference between the bearing outer race and the housing bore was applied to represent the press fit, with interference values obtained directly from experimentally measured dimensions (Tables 3–5). Axial constraint was imposed through contact with the bearing shoulder and cover, replicating assembly-induced axial restraint and preventing rigid-body motion of the bearing outer race.

Operational loads acting on the bearing housings include reaction forces from the bearing spring, gravitational loading from the rotating assembly, and centrifugal effects associated with rotor rotation. The calculation methodology for these loads is described in the subsequent force-analysis section. All loads were applied as distributed forces to reflect realistic load-transfer paths from the shaft–bearing system to the housing structure, rather than as idealised point loads.

Structural boundary conditions were applied at locations corresponding to spot welds and fasteners, thereby reproducing the constraints imposed by the fan covers. These constraints define the effective housing stiffness and differ across configurations depending on spot-weld density and rib reinforcement. All simulations were performed under quasi-static conditions, as the primary objective was to quantify elastic deformation, stress distribution, and contact pressure associated with assembly

and steady-state operation. Dynamic effects were not included in the numerical model, since vibration response was evaluated experimentally. This modelling strategy ensures consistency between numerical predictions and measured vibration and thermal behaviour.

The press fit between the bearing outer race and the housing bore was modelled using surface-to-surface frictional contact with prescribed radial interference. As an initial validation step, the nominal contact pressure induced by the interference fit was estimated analytically using classical thick-cylinder theory, as illustrated schematically in Figure 3. This analytical solution provides a baseline estimate of contact pressure assuming axisymmetric geometry and uniform material properties. The contact pressure due to interference, p, is expressed as:

$$p = \frac{\Delta D}{D} \times \frac{1}{\left[\frac{m_e - 1}{m_e E_e} - \frac{m_h - 1}{m_h E_h}\right] + 2\left[\frac{h^2}{E_e(1-h^2)} - \frac{1}{E_h\left(1-{h_o}^2\right)}\right]} \tag{1}$$

Where, $p, D, D_o, D_e, E_e, E_h, m_e, m_h, \Delta D$ are the pressure due to interference, outer ring's outer diameter of bearing, outer diameter of the housing, bearings outer ring's raceway diameter, Young's modulus of bearing, Young's modulus of housing, Poisson's ratio of bearing, Poisson's ratio of housing and interference between bearing and its housing. The h is given by:

$$h = \frac{D_e}{D}; \quad h_o = \frac{D}{D_o} \tag{2}$$

While the analytical solution assumes uniform pressure distribution, the finite element model resolves the actual contact pressure by accounting for housing compliance, geometric asymmetry, and boundary-condition-induced stiffness variations. Figure 3 illustrates the resulting contact pressure distribution on the lower bearing housing and bearing outer race obtained from the finite element analysis, highlighting deviations from the idealised uniform pressure assumed in the analytical model.

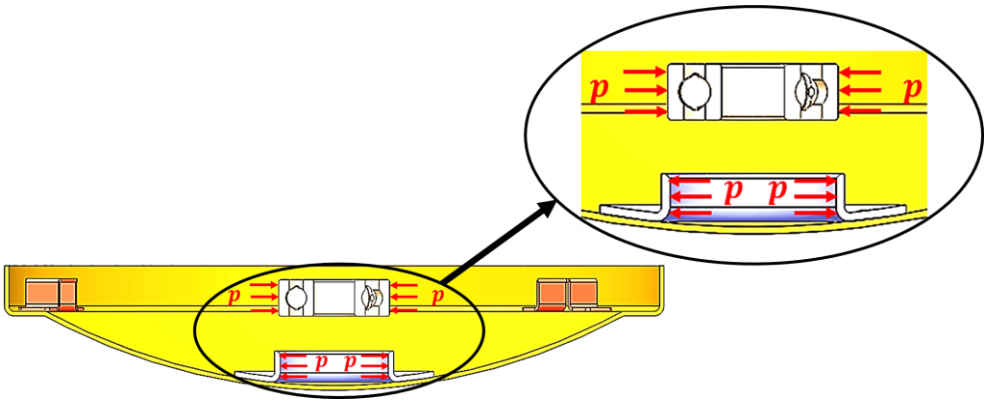

Figure 3: Pressure on the lower bearing house and ball-bearing due to interference fit.

Assembly preload arising from bolt tightening at the mounting brackets was applied to the bearing housings, as schematically illustrated in Fig. 4. These preloads introduce an initial stress state in the

housing prior to fan operation and significantly influence bearing seating, contact pressure distribution, and effective support stiffness. The axial force acting on a single mounting bracket due to bolt tightening, F_b, is given as:

$$F_b = k_b \times \Delta x_b \tag{3}$$

where k_b is the stiffness of the bracket and Δx_b is the corresponding axial deformation induced by bolt tightening. The calculated preload forces were applied as distributed loads over the bracket–housing contact regions to realistically represent load transfer and avoid artificial stress concentrations associated with point loading.

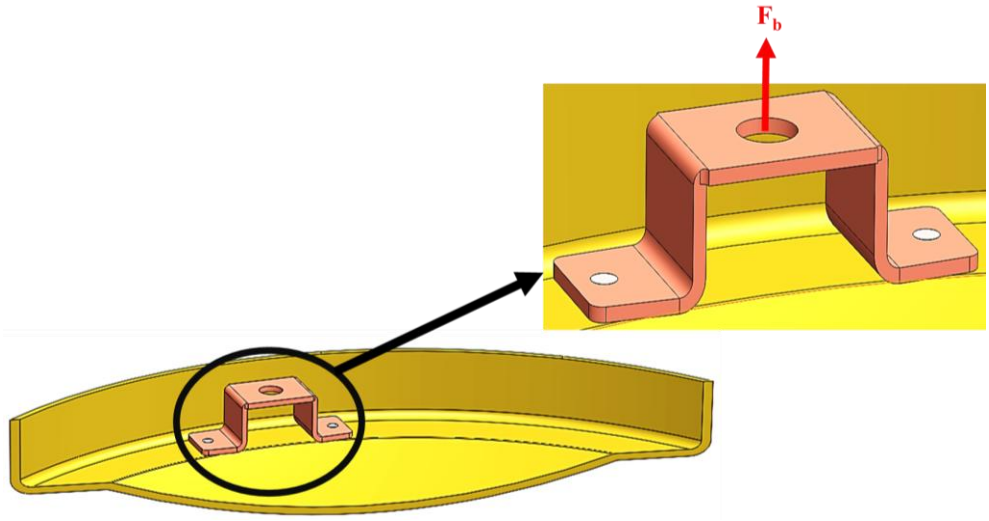

Figure 4: Force acting on one bracket due to bolt

The lower bearing is supported by a spring mechanism that generates a radial reaction force on the inner surface of the lower bearing housing. This force contributes to radial loading of the housing and directly affects bearing alignment and seating stability. The spring reaction force, F_r, applied to the housing (Fig. 5), is expressed as:

$$F_r = F = k_s \times \Delta x_s \tag{4}$$

where k_s is the spring stiffness and Δx_s is the axial compression of the spring. This force was applied as a uniformly distributed radial load along the inner circumference of the lower bearing housing in order to capture its influence on local deformation, contact pressure non-uniformity, and stress concentration at the bearing seat.

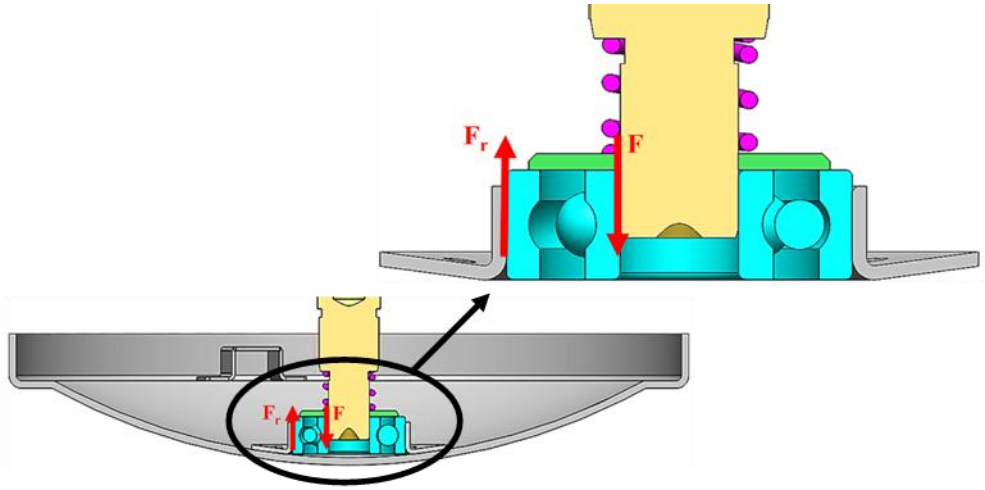

Figure 5: Shear force (F_r) acting on the inner surface of lower bearing housing as a reaction of force due to spring on the lower bearing

Centrifugal forces arising from rotor imbalance during fan operation were also considered, as illustrated in Fig. 6. A conservative single-blade imbalance scenario was adopted to evaluate housing deformation sensitivity under worst-case operating conditions. The centrifugal force generated by a single blade, F_c, is given by:

$$\mathrm{F_c} = m\, r\, \omega^2 \tag{5}$$

where m is the mass of the blade, r is the radial distance of the blade's center of mass from the axis of rotation, and ω is the angular velocity of the fan.

Force equilibrium along the spindle results in load transmission to both the upper and lower bearing housings. The corresponding radial forces acting at the centres of the upper and lower housings, $F_u$and F_l, respectively:

$$F_u = F_c \frac{l_2}{l_1 + l_2} \tag{6}$$

$$F_l = F_c \frac{l_1}{l_1 + l_2} \tag{7}$$

where, l_1, l_2 denote the axial distances from the blade to the centers of the upper and lower bearing housings, respectively. These forces were applied as equivalent distributed radial loads at the corresponding housing locations to represent realistic load transmission from the rotor–shaft assembly.

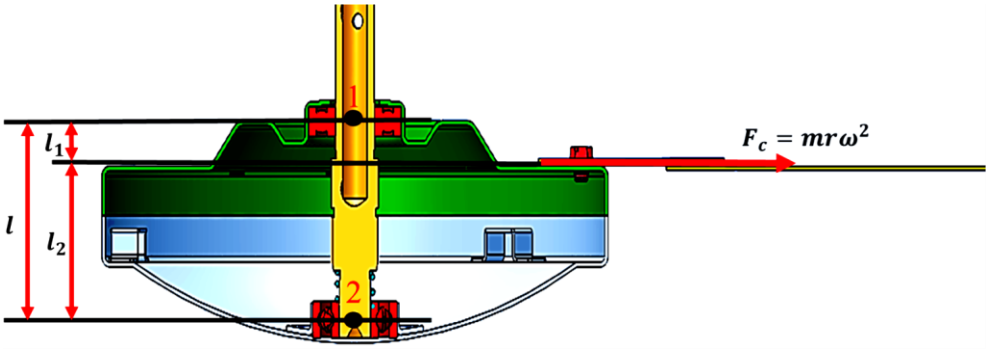

Figure 6: Centrifugal force acting on lower and upper bearing housing due to single blade

Collectively, the assembly preload, spring reaction, and centrifugal forces govern bearing housing deformation and contact pressure non-uniformity. These effects directly modulate bearing support stiffness and provide the structural basis for the vibration amplification mechanisms observed experimentally.

2.4.3. Grid independence test

The bearing housing geometries were discretized using high-quality tetrahedral finite elements. Local mesh refinement was applied in critical regions, including bearing seats, spot-weld locations, and rib intersections, where high stress gradients were anticipated. A grid independence study was conducted for representative housing configurations to ensure that predicted von Mises stress and deformation results were insensitive to mesh density. Table 6 summarizes the mesh convergence results for different combinations of spot-weld density and housing thickness. The selected meshes (highlighted in bold) represent an optimal balance between computational efficiency and numerical accuracy. Further mesh refinement resulted in changes in peak vonMises stress of < 1%, confirming numerical convergence.

Table 6: Grid independence test

S. No.	Case	Nodes	Elements	Von-Mises Stress (MPa)
1.	3 spot welds on the lower cover with thickness 1.3 mm	109,869	56,142	176.01
		223,290	126,236	175.29
		293,646	168,697	175.18
		540,584	340,023	175.15
2.	3 spot welds on the lower cover with thickness 1.6 mm	96,408	36,221	72.68
		184,270	100,025	71.77
		208,425	115,661	70.84
		293,919	171,311	70.88

3.	6 spot welds on lower cover with thickness 1.3 mm	117,347	59,467	169.09
		191,982	106,654	169.19
		193,568	106,967	169.17
		580,091	363,795	169.25
4.	6 spot welds on the lower cover with thickness 1.6 mm	211,031	118,389	72.06
		295,063	172,880	71.95
		545,064	342,824	71.97
		820,228	533,196	71.93
5.	10 spot welds on lower cover with thickness 1.3 mm	119,844	60,521	175.81
		194,710	106,841	175.46
		329,610	194,562	175.20
		591,408	369,997	175.22
6.	10 spot welds on the lower cover with thickness 1.6 mm	149,373	82,672	71.46
		235,821	137,629	71.55
		297,251	170,784	71.60
		784,185	513,817	71.59

3. Results and failure mechanism analysis

This section presents the numerical and experimental evidence used to identify the structural root cause of premature bearing degradation observed in lightly built ceiling fan assemblies. The results are interpreted from a failure-analysis perspective, linking housing deformation, contact pressure non-uniformity, vibration amplification, and temperature rise to the fretting-type damage and lubricant degradation observed in failed bearings. Each set of results is used as forensic evidence to establish how housing compliance alters bearing support conditions and initiates the coupled thermo-mechanical processes responsible for early-life bearing degradation.

3.1. Housing deformation and contact instability

The von Mises stress distributions predicted by the finite element analysis for the upper and lower bearing housings are shown in Figures 7 and 8, respectively, with corresponding peak stress and maximum deformation values summarized in Table 7. For the lower bearing housing, thin configurations with a nominal thickness of approximately 1.3 mm exhibit pronounced stress concentrations localized at the bearing seat region and at the spot-weld attachments (Figures 8a, 8c, and 8e). In these cases, predicted peak von Mises stress reaches approximately 180–210 MPa, while maximum out-of-plane deformation is on the order of 40–60 μm. These regions coincide with stiffness

discontinuities where load transfer from the rotating shaft–bearing assembly to the stationary structure occurs over limited structural paths. As a result, the applied loads are accommodated primarily through local bending of the sheet-metal housing rather than through uniform membrane action, leading to highly localized stress fields.

The dominant deformation mechanism in thin lower housings is bending of the sheet-metal structure. Under the combined influence of interference-induced contact pressure, assembly preload, spring reaction force, and centrifugal loading, the low flexural rigidity of the housing—scaling with the cube of thickness, results in bending-dominated stress fields. Increasing the lower housing thickness from approximately 1.3 mm to 1.6 mm produces a substantial reduction in predicted peak von Mises stress of approximately 35–40%, with stress levels reduced to below 120–135 MPa. The corresponding maximum deformation decreases to approximately 20–30 μm (Table 7). These results clearly identify housing thickness as the primary parameter governing global stress and deformation mitigation in the lower bearing support. By contrast, increasing the number of spot welds from three to six or ten while maintaining constant housing thickness results in only a modest reduction in peak stress, typically less than 10%, and does not significantly alter the global deformation pattern. This indicates that spot welds primarily improve local constraint and load transfer near attachment points, but do not substantially increase the overall bending stiffness of the housing. Consequently, weld density alone is insufficient to suppress deformation-induced distortion of the bearing seat in thin housing configurations.

For the upper bearing housing, Figure 7 compares configurations with and without rib reinforcement. The rib-reinforced housing exhibits a marked reduction in peak von Mises stress, decreasing from approximately 150–170 MPa in the non-reinforced configuration to below 100 MPa in the ribbed design. This reduction is accompanied by a decrease in maximum deformation from approximately 35–45 μm to 15–20 μm (Table 7). The introduction of ribs increases the effective sectional moment of inertia of the housing, suppresses local bending, and promotes a transition from bending-dominated to membrane-dominated load transfer around the bearing seat. The reduced stress concentration and deformation achieved through rib reinforcement directly limit elastic distortion of the bearing seat geometry. As demonstrated in subsequent sections, this structural stabilization plays a critical role in maintaining more uniform bearing–housing contact conditions, thereby reducing stiffness modulation effects and limiting vibration amplification during sustained operation.

Table 7: Peak vonMises stress and maximum deformation of the housing only of upper and lower bearing housings for different thickness and spot-weld configurations.

Conditions	Bearing house thickness (mm)	Maximum stress in the housing (MPa)	Maximum Total deformation in housing (µm)	Number of elements (in millions)
3 spots weld on lower bearing housing	1.295	47.449	9.315	2.25
	1.635	34.816	8.453	2.23
6 spots weld on lower bearing housing	1.295	44.887	8.808	2.13
	1.635	34.175	8.112	2.11
10 spots weld on lower bearing housing	1.295	42.644	9.050	2.12
	1.635	34.639	8.101	2.13
Upper cover without rib	1.300	130.300	37.244	1.77
Upper cover with rib	1.300	52.362	26.737	6.39

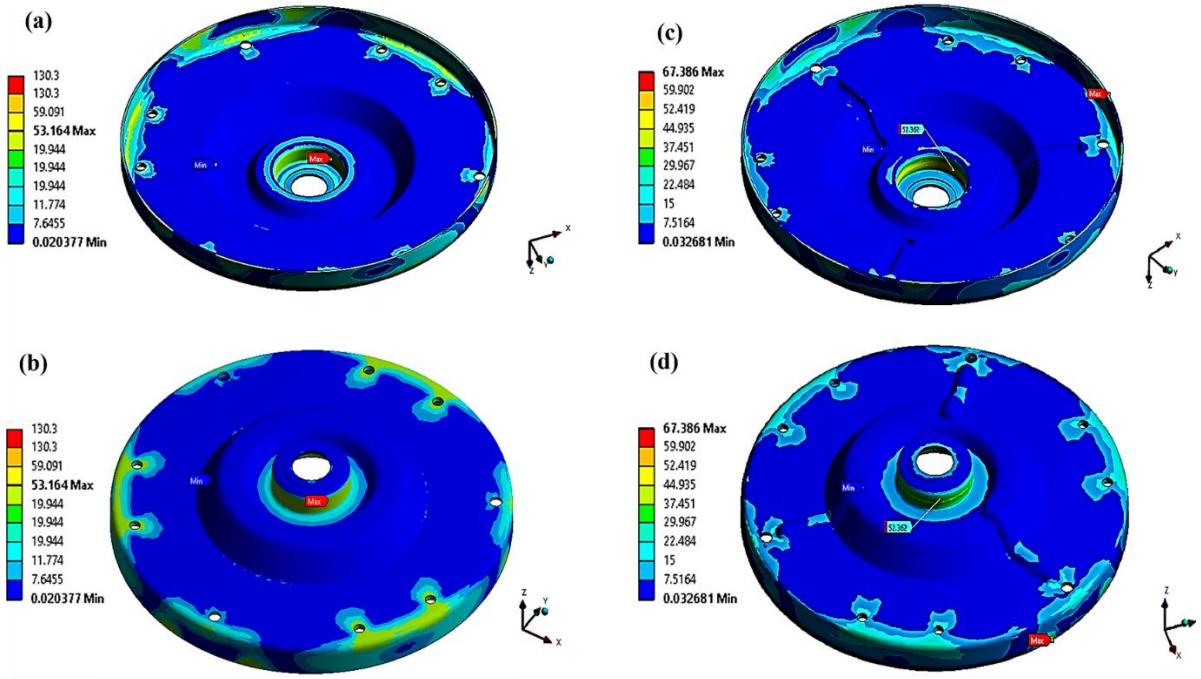

Figure 7: Von Mises stress distribution in the upper bearing housing: (a,b) configuration without rib reinforcement; (c,d) configuration with rib reinforcement.

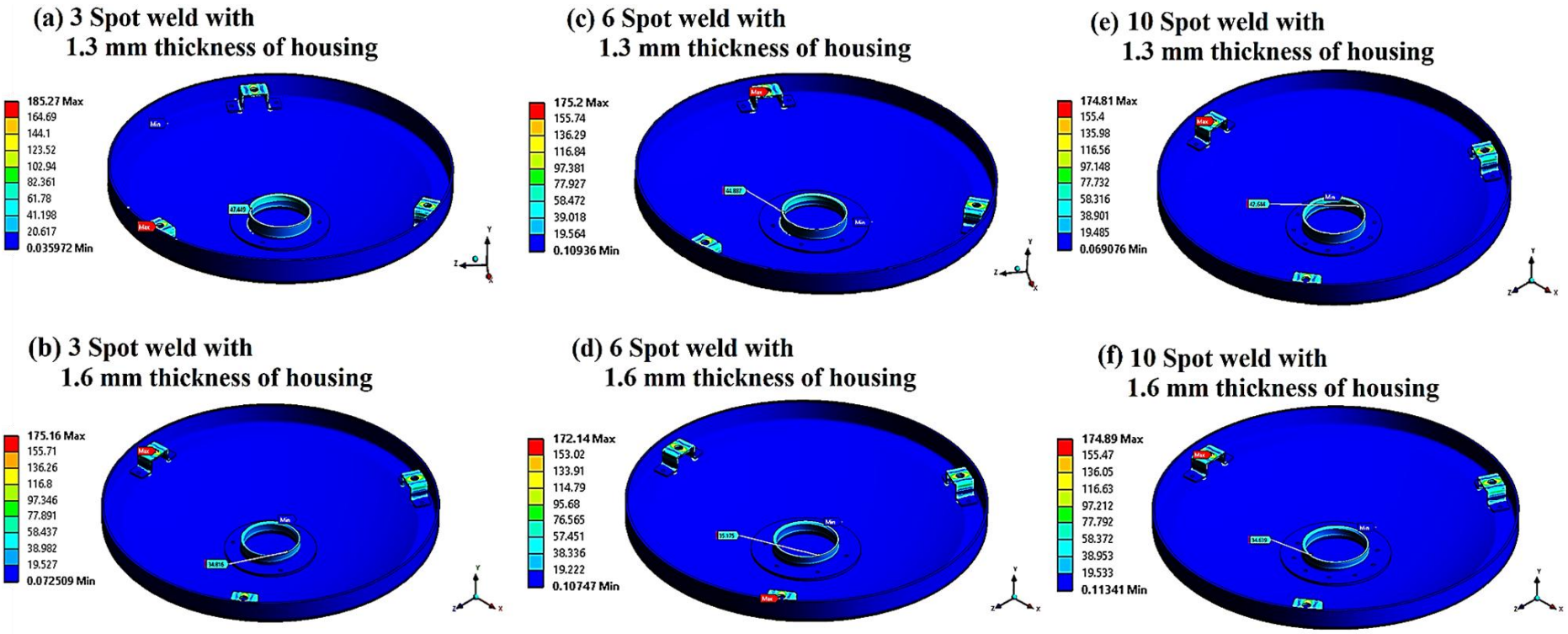

Figure 8: Von Mises stress distribution in the lower bearing housing for varying thickness and spot-weld density: (a) 3 spot welds, 1.3 mm; (b) 3 spot welds, 1.6 mm; (c) 6 spot welds, 1.3 mm; (d) 6 spot welds, 1.6 mm; (e) 10 spot welds, 1.3 mm; (f) 10 spot welds, 1.6 mm.

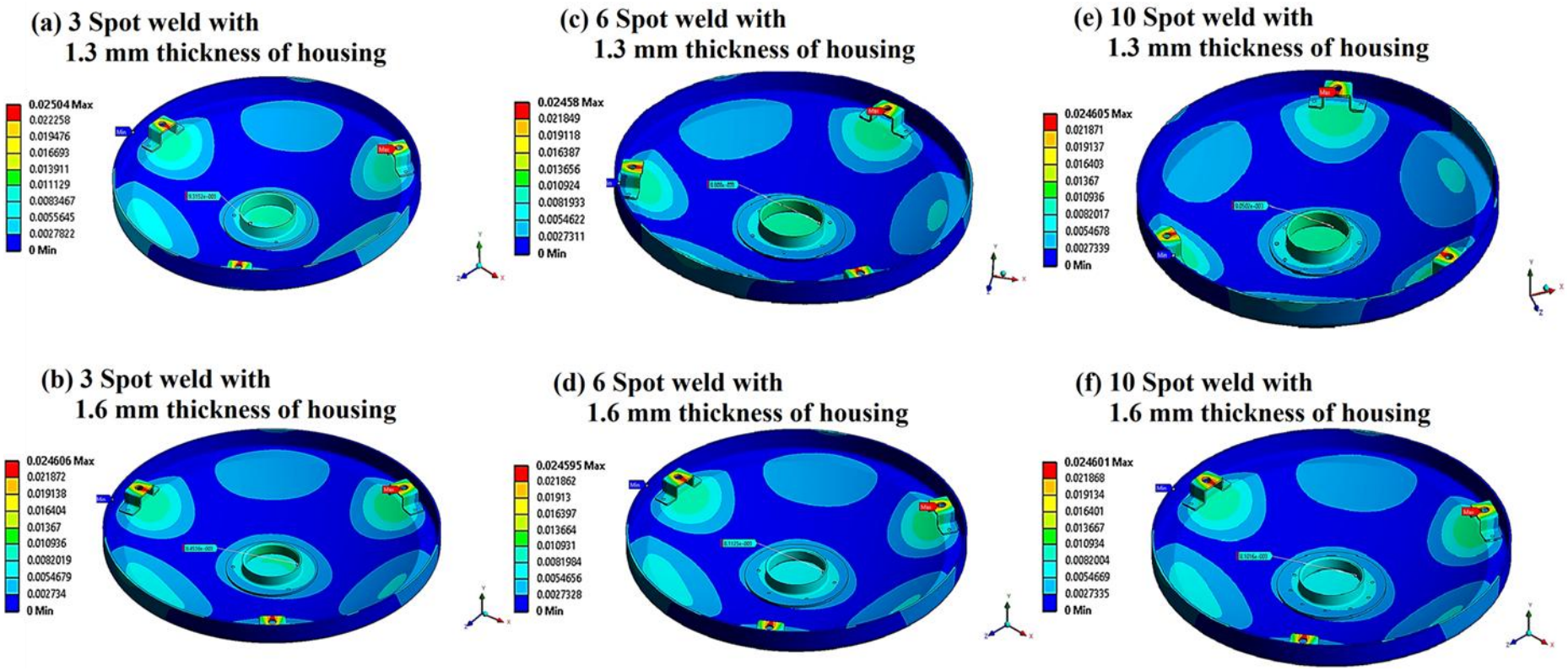

Figure 9: Total deformation (mm) in the lower bearing housing for varying thickness and spot-weld density: (a) 3 spot welds, 1.3 mm; (b) 3 spot welds, 1.6 mm; (c) 6 spot welds, 1.3 mm; (d) 6 spot welds, 1.6 mm; (e) 10 spot welds, 1.3 mm; (f) 10 spot welds, 1.6 mm.

The total deformation contours for the lower and upper bearing housings obtained from the finite element analysis are shown in Figures 9 and 10, respectively, with quantitative values summarized in Table 7. For the lower bearing housing, thin configurations exhibit pronounced elastic deformation under operational loading, with maximum radial displacement concentrated in the bearing seat region. In the thinnest configuration (nominal thickness of approximately 1.3 mm), the predicted maximum radial deformation reaches approximately 40–60 μm, depending on spot-weld density. Importantly, this deformation is non-axisymmetric, resulting in ovalisation of the bearing seat rather than uniform radial expansion.

From a contact mechanics perspective, bearing seat ovalisation disrupts circumferential load support at the bearing–housing interface. Instead of a uniform interference fit, alternating regions of elevated and reduced contact pressure develop around the bearing circumference, consistent with the non-uniform deformation patterns predicted numerically. Figures 9a, 9c, and 9e show that ovalisation is most pronounced in thin housings with reduced spot-weld density, whereas thicker housings with a nominal thickness of approximately 1.6 mm (Figures 9b, 9d, and 9f) exhibit substantially reduced deformation. In these stiffer configurations, maximum radial displacement is limited to approximately 20–30 μm and the bearing seat retains a near-circular geometry.

For the upper bearing housing, Figure 10 demonstrates that rib reinforcement significantly reduces total deformation and suppresses bearing seat distortion. The non-reinforced upper housing exhibits peak deformation on the order of 35–45 μm, while the rib-reinforced configuration limits deformation to approximately 15–20 μm under identical loading conditions (Table 7). The increased sectional stiffness provided by the ribs suppresses local bending and preserves geometric conformity between the housing bore and the bearing outer race, thereby stabilizing load transfer at the bearing–housing interface.

These deformation trends provide a direct structural explanation for the experimentally observed vibration behaviour. Configurations exhibiting greater deformation magnitude and pronounced non-axisymmetric distortion consistently correspond to higher RMS acceleration levels measured during operation. Conversely, configurations with reduced deformation and near-axisymmetric bearing support exhibit lower and more stable vibration magnitudes. The results demonstrate that housing deformation magnitude and symmetry, rather than nominal bearing load capacity, govern bearing support uniformity and stiffness modulation, which in turn control vibration amplification in low-cost ceiling fan systems. Such non-axisymmetric deformation of the bearing seat is mechanically consistent with the fretting marks and non-uniform wear patterns observed on bearing outer races during post-service inspection of failed units.

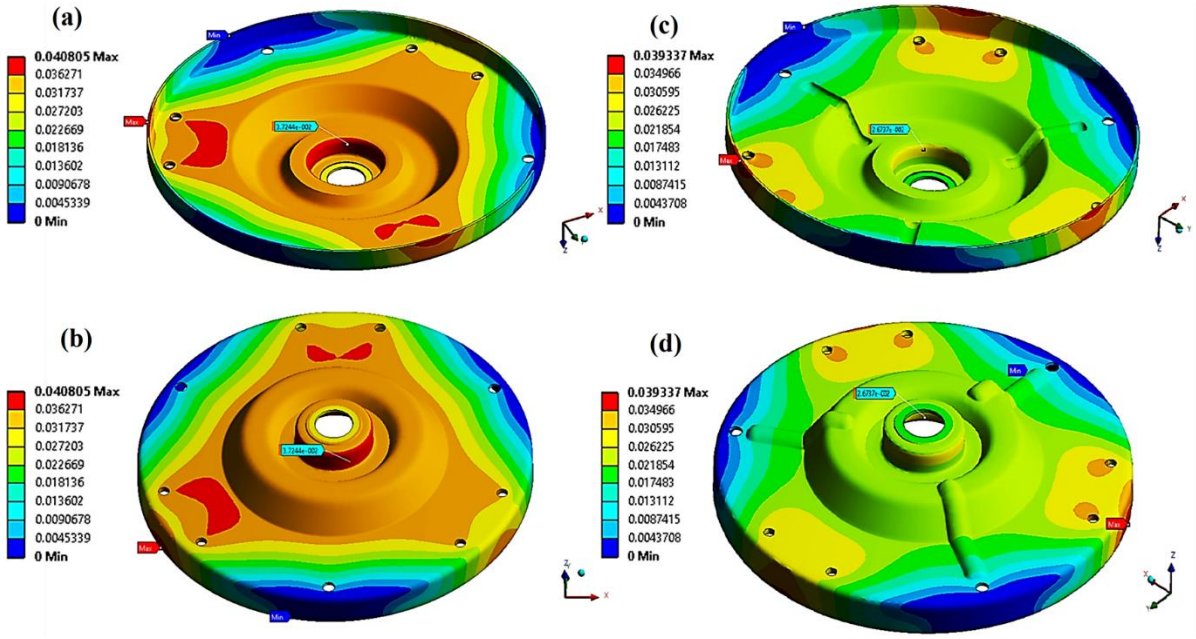

Figure 10: Total deformation contours of the upper bearing housing: (a,b) without rib reinforcement; (c,d) with rib reinforcement.

3.2. Effect of interference fit on contact pressure and micro-slip behaviour

The measured interference values between the bearing outer races and the bearing housings, together with the experimentally observed temperature rise at the bearing covers, are summarised in Table 8. Across the investigated configurations, the bearing–housing interference fit ranges approximately from 10 to 25 μm, depending on housing thickness, spot-weld configuration, and bearing internal clearance class. While these interference levels fall within typical manufacturing tolerances for press-fitted bearings, their mechanical effect is shown to be strongly dependent on housing stiffness.

Numerical contact analysis reveals that, in compliant housing configurations, relatively high interference fits within this range lead to strongly non-uniform contact pressure distributions. Peak local contact pressures increase by approximately 25–35% compared with fully reinforced housings, with pressure concentrations occurring preferentially in regions where housing deformation is locally constrained by spot welds or geometric features. Adjacent regions experience reduced contact pressure or partial loss of contact as a result of bearing seat ovalisation. These pressure gradients indicate unstable bearing support conditions rather than uniform circumferential load sharing.

Under steady-state operation, the combined effects of cyclic loading and vibration promote relative micro-motion at the bearing–housing interface in these non-uniform contact regions. Such micro-slip is mechanically consistent with classical fretting mechanisms, in which repeated small-amplitude relative motion under elevated contact pressure leads to increased frictional dissipation and surface damage. Although direct measurement of micro-slip was not performed, the presence of highly non-uniform contact pressure provides a clear mechanical basis for its occurrence in compliant housings.

The experimentally measured temperature rise supports this interpretation. Thin, non-reinforced housing configurations exhibit significantly higher temperature increases, typically in the range of 8–12 °C above ambient at the bearing covers (Table 8). This elevated thermal response is consistent with increased frictional energy dissipation associated with contact instability and micro-slip at the bearing–housing interface. In contrast, reinforced housings achieved through increased housing thickness and ribbed upper covers exhibit smoother contact pressure distributions and substantially lower temperature rise, typically limited to approximately 3–5 °C under identical operating conditions.

These results demonstrate that interference fit cannot be selected independently of housing stiffness in lightly built rotating machinery. While increased interference is often employed to improve bearing retention, excessive interference in compliant housings exacerbates contact pressure non-uniformity, promotes micro-slip, and increases frictional heating, ultimately degrading vibration and thermal performance. Effective control of bearing behaviour therefore requires coordinated optimization of both housing stiffness and interference fit, rather than reliance on interference alone. This explains why bearings replaced in the same housing often fail repeatedly in field applications.

Table 8: Interference fit parameters and experimentally measured temperature rise at upper and lower bearing housings for different bearing clearances and housing configurations

Conditions	Temp. rise at the lower bearing cover (^{0}C)	Temp. rise at the upper bearing cover (^{0}C)	Clearance	Bearing number (SKF)	Calculated radial fit value between bearing and spindle (µm)	Calculated radial fit value between bearing and housing (µm)
3 spots weld on the lower bearing housing and no rib on the upper cover	60.6	40.6	CN	6201	-50	-13
				6202	-40	-173
	59.7	42.7	C3	6201	-40	-11
				6202	+20	-183
3 spots weld on the lower bearing housing and rib on the upper cover	55.9	40.9	CN	6201	-63	-125
				6202	-30	-188
	57.2	43.2	C3	6201	- 30	- 115
				6202	- 20	- 188
6 spots weld on the lower bearing housing and	56.2	43.2	CN	6201	- 40	- 273
				6202	- 40	- 203

no rib on the upper cover	57.5	41.5	C3	6201	- 50	- 631
				6202	- 20	- 145
6 spots weld on the lower bearing housing and rib on the upper cover	57.4	36.4	CN	6201	00	-283
				6202	-30	-298
	59.5	39.5	C3	6201	-20	-183
				6202	-30	-298

The negative sign (Table 8) indicates clearance direction based on sign convention. The magnitude represents calculated dimensional deviation used as simulation input and does not represent physical radial interference.

3.3. Vibration response characteristics under varying housing stiffness

Figures 11–14 present the experimentally measured vibration response in terms of RMS acceleration, expressed as the ratio of vibration magnitude for C3-clearance bearings relative to CN-clearance bearings. The ratios are evaluated in both the time and frequency domains at operating durations of 20, 40, and 60 minutes to isolate the influence of bearing internal clearance under different housing stiffness configurations while minimizing test-to-test variability in absolute signal levels.

For the stiffest configuration, comprising six spot welds in the lower housing and rib reinforcement in the upper cover (Figure 11), the vibration response remains stable over the full operating duration. Absolute RMS acceleration magnitudes remain low, typically within 0.4–0.6 m/s², and the C3/CN ratio remains close to unity at all time intervals. This behaviour is consistent with the numerical predictions presented in Section 3.1, which show minimal bearing seat deformation and near-axisymmetric contact pressure distributions for reinforced housings. The absence of broadband growth in the frequency-domain response indicates that increased bearing clearance does not induce vibration amplification when the bearing support stiffness is sufficiently high and contact pressure remains uniform.

When rib reinforcement is removed from the upper cover while retaining six spot welds in the lower housing (Figure 12), a measurable increase in vibration magnitude is observed. Absolute RMS acceleration levels rise to approximately 0.6–0.9 m/s², and the C3/CN ratio consistently exceeds unity, with a gradual increase over operating time. Frequency-domain spectra exhibit broadband energy amplification rather than discrete tonal components. This response correlates directly with the FE results showing increased housing deformation and the onset of contact pressure non-uniformity, indicating that partial loss of structural stiffness introduces stiffness modulation at the bearing support.

The most compliant configuration, involving three spot welds in the lower housing without rib reinforcement (Figure 13), exhibits the highest vibration magnitudes and the strongest clearance sensitivity. RMS acceleration levels reach approximately 0.9–1.2 m/s², and the C3/CN ratio is significantly greater than unity even at early operating times. Pronounced broadband amplification is observed in the frequency domain, consistent with severe bearing seat ovalisation and highly non-uniform contact pressure distributions predicted numerically. In this configuration, rolling elements repeatedly traverse regions of alternating high and low support stiffness, producing a parametric excitation mechanism that amplifies broadband vibration energy rather than discrete bearing characteristic frequencies.

Figure 14 shows that adding rib reinforcement to the upper cover partially mitigates vibration amplification for the three-spot-weld lower housing. Absolute RMS acceleration levels are reduced to approximately 0.7–1.0 m/s², and the growth rate of the C3/CN ratio is moderated. However, vibration levels remain substantially higher than those observed for the fully reinforced configuration. This outcome is consistent with FE results indicating that rib reinforcement alone cannot fully suppress bearing seat distortion when the lower housing remains highly compliant.

Overall, the results demonstrate that housing stiffness governs both the absolute vibration magnitude and the sensitivity of vibration response to bearing internal clearance. Configurations exhibiting larger FE-predicted deformation and non-uniform contact pressure consistently show higher RMS vibration levels and stronger time-dependent amplification. From an engineering standpoint, these findings confirm that vibration control in lightly loaded rotating machinery is primarily a structural problem: adequate reinforcement of bearing housings is essential to suppress stiffness modulation effects and to decouple vibration response from bearing internal clearance selection. This behaviour explains why conventional vibration-based bearing diagnostics relying on defect frequencies fail to detect early degradation in such systems, as the dominant vibration signature arises from structurally induced broadband excitation rather than localized bearing defects.

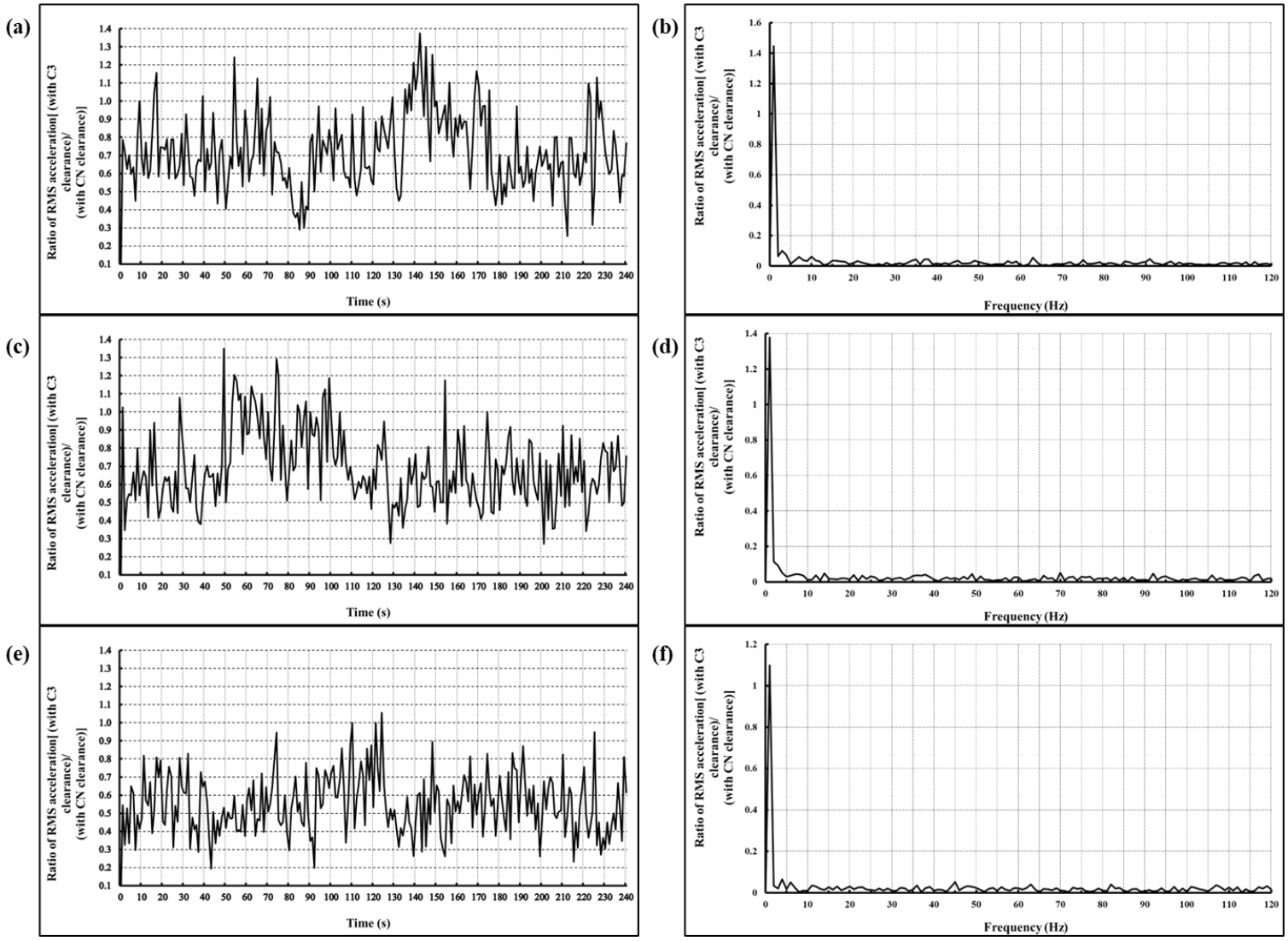

Figure 11: Ratio of RMS acceleration [(with C3 clearance)/ (with CN clearance)] for 6 spots weld & rib on top cover -vs- Time in (a) for 20 minutes (c) for 40 minutes (e) for 60 minutes. Ratio of RMS acceleration [(with C3 clearance)/ (with CN clearance)] for 6 spots weld & rib on top cover -vs- Frequency in (b) for 20 minutes (d) for 40 minutes (f) for 60 minutes.

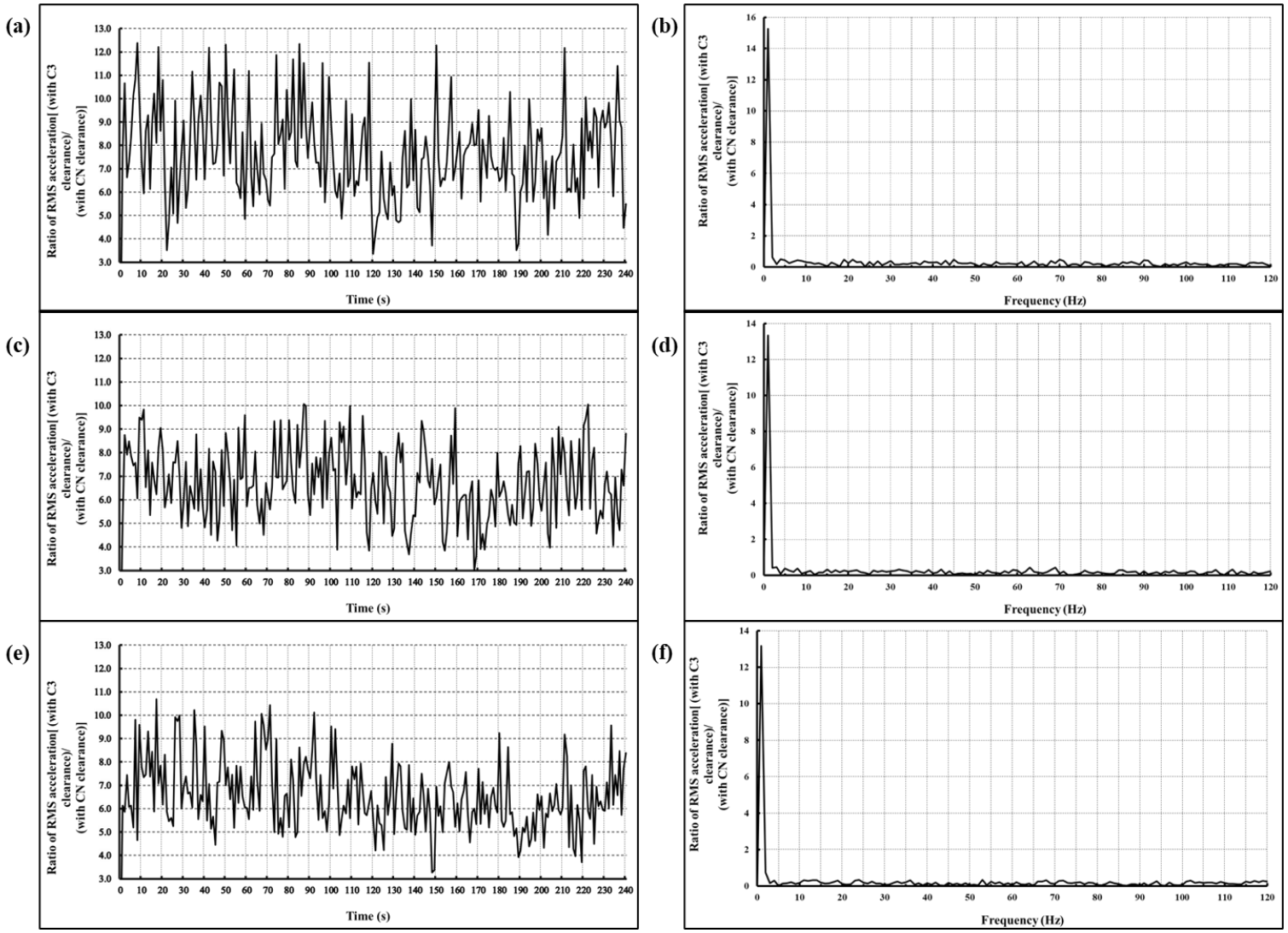

Figure 12: Ratio of RMS acceleration [(with C3 clearance)/ (with CN clearance)] for 6 spots weld & no rib on top cover -vs- Time in (a) for 20 minutes (c) for 40 minutes (e) for 60 minutes. Ratio of RMS acceleration [(with C3 clearance)/ (with CN clearance)] for 6 spots weld & no rib on top cover -vs- Frequency in (b) for 20 minutes (d) for 40 minutes (f) for 60 minutes.

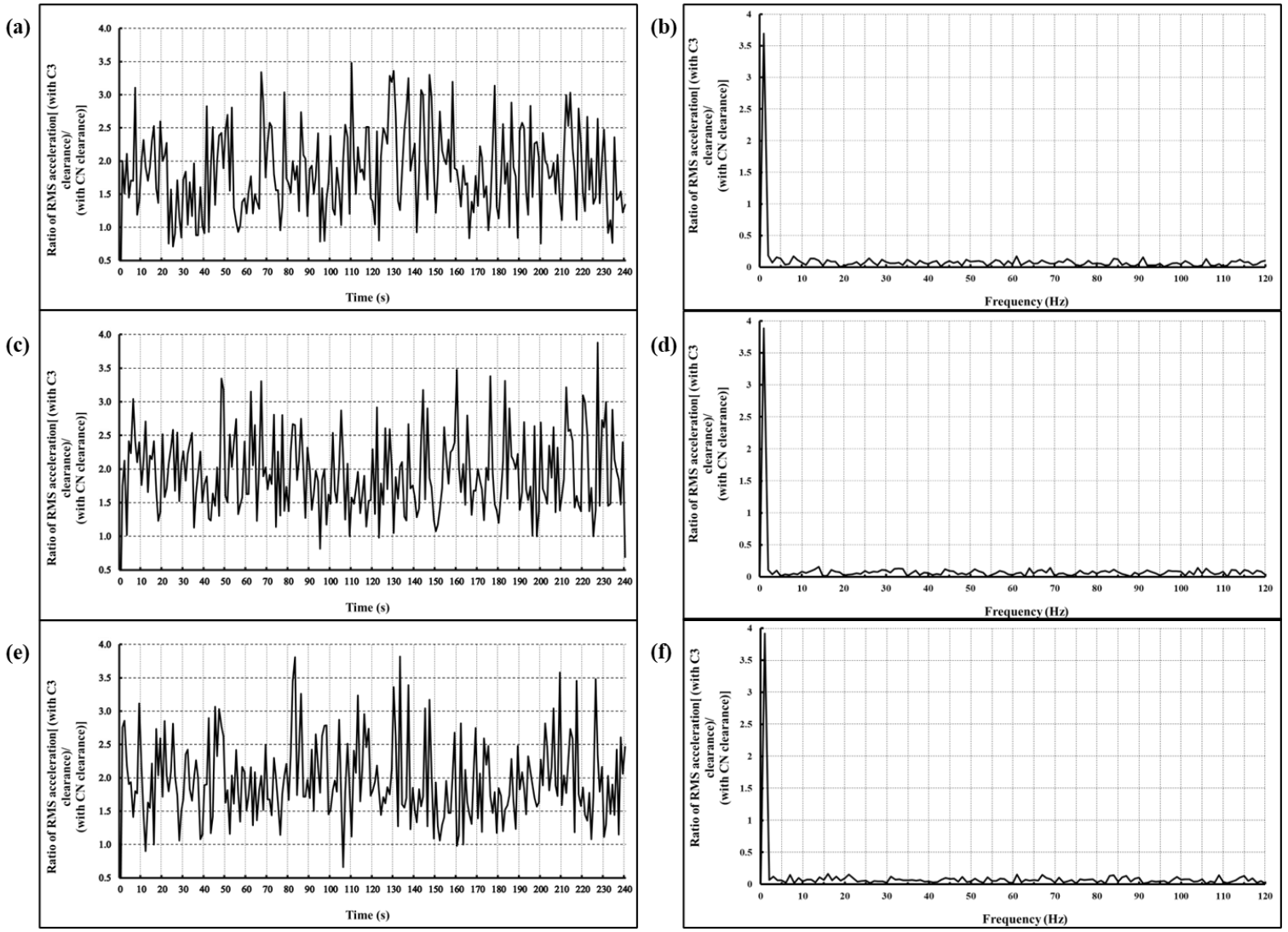

Figure 13: Ratio of RMS acceleration [(with C3 clearance)/ (with CN clearance)] for 3 spots weld & no rib on top cover -vs- Time in (a) for 20 minutes (c) for 40 minutes (e) for 60 minutes. Ratio of RMS acceleration [(with C3 clearance)/ (with CN clearance)] for 3 spots weld & no rib on top cover -vs- Frequency in (b) for 20 minutes (d) for 40 minutes (f) for 60 minutes.

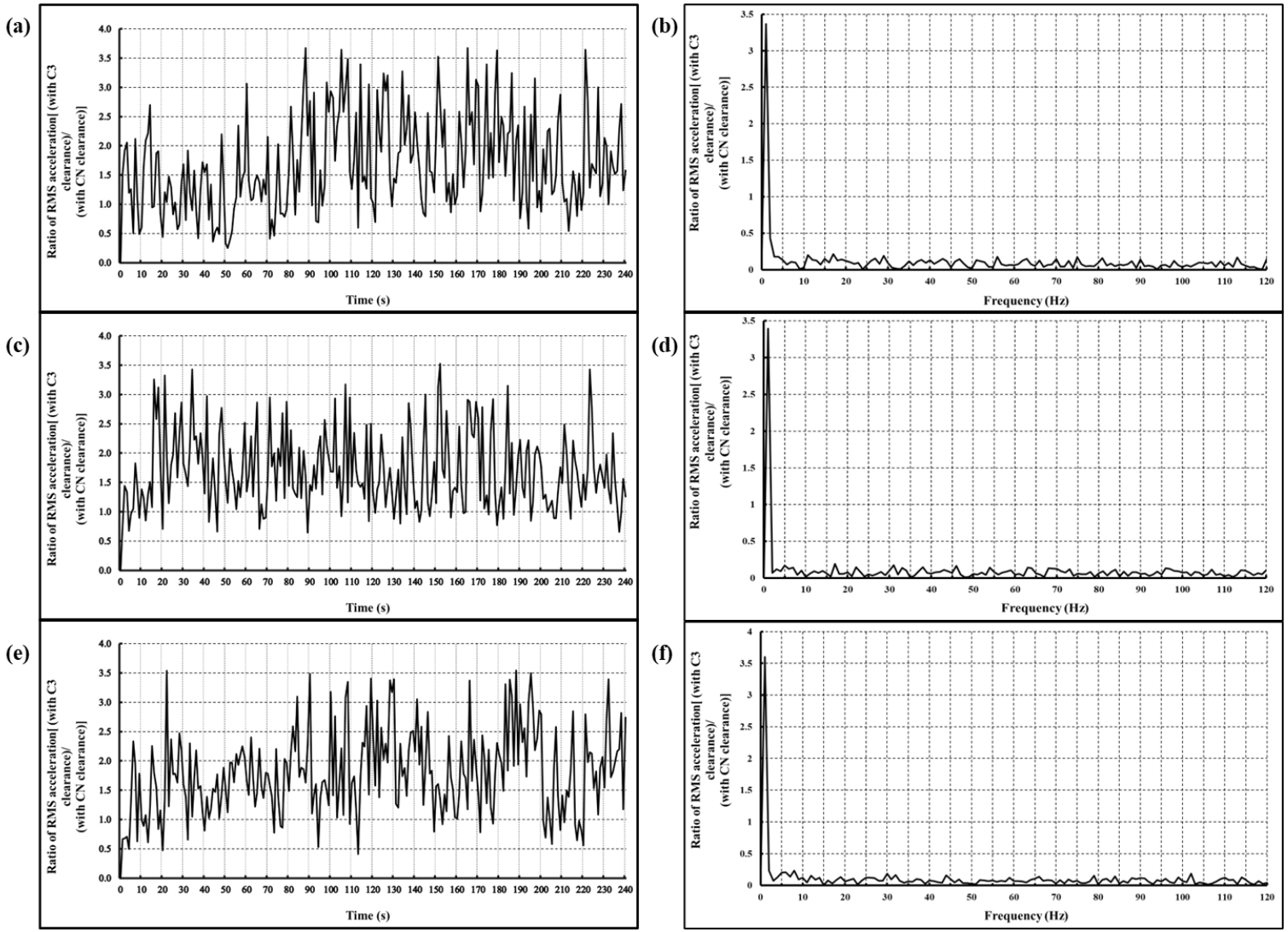

Figure 14: Ratio of RMS acceleration [with C3 clearance)/ (with CN clearance)] for 3 spots weld & rib on top cover -vs- Time in (a) for 20 minutes (c) for 40 minutes (e) for 60 minutes. Ratio of RMS acceleration [(with C3 clearance)/ (with CN clearance)] for 3 spots weld & rib on top cover -vs- Frequency in (b) for 20 minutes (d) for 40 minutes (f) for 60 minutes.

3.4. Thermal response and friction-induced heating mechanisms

The bearing housing temperature rise summarized in Table 8 exhibits a strong correlation with both vibration amplitude (Figure 11) and numerically predicted housing deformation (Figures 9 and 10). Thin housing configurations combined with relatively high interference fits show the highest temperature rise, with measured increases of approximately 8–12 °C above ambient. In contrast, reinforced housing configurations limit the temperature rise to approximately 3–5 °C under identical operating conditions.

This pronounced temperature elevation in compliant housings indicates substantially increased frictional heat generation and arises from two coupled mechanisms. First, finite element contact analysis reveals highly non-uniform contact pressure distributions in compliant housings, with localized pressure peaks caused by bearing seat ovalization. Under cyclic operational loading, these pressure gradients promote micro-slip at the bearing–housing interface, increasing frictional dissipation. Second, constrained thermal expansion of the bearing outer race within a deformable housing increases effective bearing preload during operation, elevating rolling and sliding losses within the bearing. These mechanisms act synergistically, producing a rapid increase in operating temperature once steady-state conditions are reached.

Housing configurations with increased stiffness, achieved through greater sheet thickness, higher spot-weld density, and rib-reinforced upper covers, exhibit significantly lower temperature rise and more stable thermal behaviour. Bearings with increased internal clearance (C3) generally reduce operating temperature by approximately 1–3 °C relative to CN bearings; however, Table 8 shows that this effect is secondary to housing stiffness. Without adequate structural rigidity, clearance modification alone is insufficient to prevent thermal escalation driven by contact instability at the bearing–housing interface.

3.5. Coupled degradation mechanism

By integrating numerical predictions (Figures 7–10, Tables 7 and 8) with experimental vibration measurements (Figure 11), a coupled degradation mechanism governing bearing performance in compliant housings can be established. Housing compliance induces elastic bearing seat ovalization on the order of tens of micrometers, leading to non-uniform contact pressure and periodic stiffness variation as rolling elements traverse regions of differing support stiffness.

This stiffness modulation promotes micro-slip at the bearing–housing interface and results in broadband vibration amplification of approximately 40–60% relative to reinforced configurations. The associated increase in frictional heat generation produces elevated operating temperatures, which accelerate lubricant degradation by reducing effective viscosity and load-carrying capacity. The resulting shift toward mixed or boundary lubrication further increases frictional losses and vibration levels, reinforcing the thermo-mechanical–vibratory coupling.

Over extended service periods, this positive feedback loop drives bearing degradation well before classical rolling-contact fatigue limits are reached, even in the absence of localized raceway or rolling-element defects. This mechanism provides a mechanistic explanation for the premature bearing failures frequently observed in low-cost ceiling fan applications and other lightly built rotating machinery. The results demonstrate that bearing degradation in such systems is governed as much by structural compliance and thermo-mechanical interaction as by traditional bearing life considerations.

4. Conclusions

This investigation demonstrates that many premature bearing failures in lightly built rotating machinery are incorrectly attributed to bearing defects, whereas the true root cause is structural compliance of the bearing housing:

- Finite element analysis shows that thin, weakly reinforced bearing housings undergo bending-dominated deformation, producing non-axisymmetric bearing seat ovalization of approximately 40–60 μm. This deformation results in highly non-uniform contact pressure distributions and local peak contact stress increases of approximately 30% compared with reinforced housings.
- Experimental measurements confirm that configurations exhibiting pronounced housing deformation experience 40–60% higher RMS vibration levels and bearing housing temperature rises of 8–12 °C, relative to fully reinforced configurations under identical operating conditions.
- Non-uniform contact pressure and cyclic stiffness variation promote micro-slip and fretting-type behaviour at the bearing–housing interface, increasing frictional heat generation and accelerating lubricant degradation. This process shifts the bearing toward mixed or boundary lubrication, further amplifying vibration and thermal response.
- A coupled degradation mechanism is established in which housing compliance initiates contact instability, leading to a positive thermo-mechanical–vibratory feedback loop that accelerates bearing degradation well before classical rolling-contact fatigue limits are reached.
- These findings explain premature bearing failures frequently observed in low-cost ceiling fan assemblies and similar lightly supported rotating systems. The results highlight the necessity of treating bearing housing stiffness as a critical reliability parameter and caution against attributing early-life bearing failures solely to bearing quality or manufacturing variability.

Overall, the results demonstrate that housing stiffness is the dominant design parameter controlling vibration magnitude, thermal stability, and bearing durability in lightly built rotating machinery. Structural reinforcement of bearing housings offers a robust and cost-effective strategy for reducing

RMS vibration by up to 50% and limiting temperature rise by 5–8 °C. Future vibration-based diagnostic and prognostic frameworks for low-cost rotating systems must explicitly account for housing compliance effects, as structurally induced broadband excitation can dominate early vibration signatures and obscure conventional defect-frequency indicators.

Declaration of Competing Interest

The authors declare that they have no known competing financial interests or personal relationships that could have appeared to influence the work reported in this paper.

Acknowledgements

During the preparation of this manuscript, the authors used ChatGPT to assist with language editing and clarity. After using this tool, the authors critically reviewed and revised the content and take full responsibility for the integrity and originality of the published work.

Author Contributions

Neha Pandey: Methodology, Experimental investigation, Data curation, Formal analysis, Visualization, Writing – original draft.

Deepak K. Pandey: Conceptualization, Supervision, Numerical modelling, Validation, Writing – review & editing.

Data availability

The data supporting this study's findings are available from the corresponding author upon reasonable request.

References

[1] M.G. Kent, T. Cheung, J. Li, S. Schiavon, Experimental evaluation of visual flicker caused by ceiling fans, Build. Environ. 182 (2020). https://doi.org/10.1016/j.buildenv.2020.107060.

[2] S. Omrani, S. Matour, K. Bamdad, N. Izadyar, Ceiling fans as ventilation assisting devices in buildings: A critical review, Build. Environ. 201 (2021). https://doi.org/10.1016/j.buildenv.2021.108010.

[3] F. Trebuňa, F. Šimčák, J. Bocko, R. Huňady, M. Pástor, Complex approach to the vibrodiagnostic analysis of excessive vibration of the exhaust fan, Eng. Fail. Anal. 37 (2014) 86–95. https://doi.org/10.1016/j.engfailanal.2013.11.015.

[4] N. Tandon, A. Choudhury, A review of vibration and acoustic measurement methods for the detection of defects in rolling element bearings, Tribol. Int. 32 (1999) 469–480. https://doi.org/10.1016/S0301-679X(99)00077-8.

[5] R.K. Upadhyay, L.A. Kumaraswamidhas, M.S. Azam, Rolling element bearing failure analysis: A case study, Case Stud. Eng. Fail. Anal. 1 (2013) 15–17. https://doi.org/10.1016/J.CSEFA.2012.11.003.

[6] P. Gupta, M.K. Pradhan, Fault detection analysis in rolling element bearing: A review, Mater. Today Proc. 4 (2017) 2085–2094. https://doi.org/10.1016/j.matpr.2017.02.054.

[7] T.A. Harris, M.N. Kotzalas, Advanced Concepts of Bearing Technology: Rolling Bearing Analysis, Fifth Edition, CRC Press, 2021.

[8] SKF, Rolling bearings, 2018.

[9] I. Salam, A. Tauqir, A.U.L. Haq, A.Q. Khan, AN AIR CRASH DUE TO FATIGUE FAILURE OF A BALL BEARING, Eng. Fail. Anal. 5 (1998). https://doi.org/https://doi.org/10.1016/B978-0-08-043959-4.50042-0.

[10] N. Sawalhi, R.B. Randall, H. Endo, The enhancement of fault detection and diagnosis in rolling element bearings using minimum entropy deconvolution combined with spectral kurtosis, Mech. Syst. Signal Process. 21 (2007) 2616–2633. https://doi.org/10.1016/j.ymssp.2006.12.002.

[11] M. Wang, K. Yan, X. Zhang, Y. Zhu, J. Hong, A comprehensive study on dynamic performance of ball bearing considering bearing deformations and ball-inner raceway separation, Mech. Syst. Signal Process. 185 (2023) 109826. https://doi.org/10.1016/j.ymssp.2022.109826.

[12] R.B. Waterhouse, Fretting fatigue, International Materials Reviews 37 (1992) 77–98. https://doi.org/10.1179/imr.1992.37.1.77.

[13] O. Vingsbo, S. Söderberg, On fretting maps, Wear 126 (1988) 131–147. https://doi.org/10.1016/0043-1648(88)90134-2.

[14] I.R. McColl, J. Ding, S.B. Leen, Finite element simulation and experimental validation of fretting wear, Wear 256 (2004) 1114–1127. https://doi.org/10.1016/j.wear.2003.07.001.

[15] A. Harnoy, Bearing Design in Machinery, Bearing Design in Machinery (2002). https://doi.org/10.1201/9780203909072.

[16] P. Raftery, J. Fizer, W. Chen, Y. He, H. Zhang, E. Arens, S. Schiavon, G. Paliaga, Ceiling fans: Predicting indoor air speeds based on full scale laboratory measurements, Build. Environ. 155 (2019) 210–223. https://doi.org/10.1016/j.buildenv.2019.03.040.

[17] F. Babich, M. Cook, D. Loveday, R. Rawal, Y. Shukla, Transient three-dimensional CFD modelling of ceiling fans, Build. Environ. 123 (2017) 37–49. https://doi.org/10.1016/j.buildenv.2017.06.039.

[18] S.H. Ho, L. Rosario, M.M. Rahman, Thermal comfort enhancement by using a ceiling fan, Appl. Therm. Eng. 29 (2009) 1648–1656. https://doi.org/10.1016/J.APPLTHERMALENG.2008.07.015.

[19] H.M. Lee, K.M. Lim, H.P. Lee, Reduction of Ceiling Fan Noise by Serrated Trailing Edge, Fluctuation and Noise Letters 17 (2018) 1850026. https://doi.org/10.1142/S0219477518500268.